https://doi.org/10.3847/1538-4357/ac5f41

Multiwavelength and Multi-CO View of the Minor Merger Driven Star Formation in the Nearby LIRG NGC 3110

Yuka Kawana[1,2], Toshiki Saito[3,4,5], Sachiko K. Okumura[2], Ryohei Kawabe[4], Daniel Espada[6], Daisuke Iono[4,7], Hiroyuki Kaneko[4,8], Minju M. Lee[9], Tomonari Michiyama[4,10], Kentaro Motohara[4,11], Kouichiro Nakanishi[4,7], Alex R. Pettitt[12], Zara Randriamanakoto[13,14], Junko Ueda[4], and Takuji Yamashita[4]

[1] Tokyo Metropolitan Mihara High School, 1-33-1 Omorihigashi, Ota-ku, Tokyo, Japan; toshiki.saito@nao.ac.jp, saito.toshiki@nihon-u.ac.jp
[2] Japan Women's University, 2-8-1 Mejirodai, Bunkyo-ku, Tokyo 112-8681, Japan
[3] Department of Physics, General Studies, College of Engineering, Nihon University, 1 Nakagawara, Tokusada, Tamuramachi, Koriyama, Fukushima 963-8642, Japan
[4] National Astronomical Observatory of Japan, 2-21-1 Osawa, Mitaka, Tokyo 181-8588, Japan
[5] Max-Planck-Institut für Astronomie, Königstuhl 17, D-69117, Heidelberg, Germany
[6] Departamento de Física Teórica y del Cosmos, Campus de Fuentenueva, Universidad de Granada, E-18071 Granada, Spain
[7] The Graduate University for Advanced Studies (SOKENDAI), 2-21-1 Osawa, Mitaka, Tokyo 181-0015, Japan
[8] Graduate School of Education, Joetsu University of Education, 1, Yamayashiki-machi, Joetsu, Niigata 943-8512, Japan
[9] Max-Planck-Institut für Extraterrestrische Physik, Giessenbachstraße, D-85748, Garching, Germany
[10] Department of Earth and Space Science, Osaka University, 1-1 Machikaneyama, Toyonaka, Osaka 560-0043, Japan
[11] Institute of Astronomy, The University of Tokyo, 2-21-1 Osawa, Mitaka, Tokyo 181-0015, Japan
[12] Department of Physics, Faculty of Science, Hokkaido University, Kita 10 Nishi 8 Kita-ku, Sapporo, Hokkaido 060-0810, Japan
[13] South African Astronomical Observatory, PO Box 9, Observatory 7935, Cape Town, South Africa
[14] Department of Physics, University of Antananarivo, P.O. Box 906, Antananarivo, Madagascar
Received 2021 July 2; revised 2022 February 17; accepted 2022 March 19; published 2022 April 18

Abstract

We present Atacama Large Millimeter/submillimeter Array observations of multiple ^{12}CO, ^{13}CO, and C^{18}O lines and 2.9 mm and 1.3 mm continuum emission toward the nearby interacting luminous infrared galaxy NGC 3110, supplemented with similar spatial resolution Hα, 1.4 GHz continuum, and K-band data. We estimate the typical CO-to-H$_2$ conversion factor of 1.7 $M_\odot$ (K km s^{-1} pc^2)$^{-1}$ within the disk using local thermal equilibrium-based and dust-based H$_2$ column densities, and measure the 1 kpc scale surface densities of the star formation rate ($\Sigma_{\rm SFR}$), super star clusters ($\Sigma_{\rm SSC}$), molecular gas mass, and star formation efficiency (SFE) toward the entire gas disk. These parameters show a peak in the southern part of the southern spiral arm (SFE $\sim 10^{-8.2}$ yr^{-1}, $\Sigma_{\rm SFR} \sim 10^{-0.6} M_\odot$ kpc^{-2} yr^{-1}, $\Sigma_{\rm SSC} \sim 6.0$ kpc^{-2}), which is likely attributable to the ongoing tidal interaction with the companion galaxy MCG-01-26-013, as well as toward the circumnuclear region. We also find that thermal free–free emission contributes to a significant fraction of the millimeter continuum emission at the position of the southern peak. These measurements imply that the peak of the southern arm is an active and young star-forming region, whereas the central part of NGC 3110 is a site of long-continued star formation. We suggest that during the early stage of the galaxy–galaxy interaction in which the mass ratio was high in NGC 3110, fragmentation along the main galaxy arms is an important driver of merger-induced star formation, and that massive gas inflow results in dusty nuclear starbursts.

Unified Astronomy Thesaurus concepts: Galaxy pairs (610); Infrared excess galaxies (789); Radiative transfer (1335); Starburst galaxies (1570); Scaling relations (2031); Molecular spectroscopy (2095)

1. Introduction

Studying star formation processes in various galaxies provides us information that is critical to unveil how galaxies are formed and evolved in time and thus to investigate the origin of the Hubble sequence (Hubble 1926; Kennicutt 1998a). When two galaxies approach each other, they exert tidal forces and change their morphology. In the case of gas-rich galaxies, large-scale inflow supplies molecular gas to the central regions, resulting in the burst of nuclear star formation (e.g., Barnes & Hernquist 1992; Mihos & Hernquist 1996). On the other hand, recent observational and theoretical works have revealed that at the early to mid stage of the interaction, merger-driven star formation is more dominated by gas fragmentation across the progenitor's disks (e.g., Teyssier

et al. 2010; Elmegreen et al. 2017; Pettitt et al. 2017; Tomičić et al. 2018), or in a filamentary structure between the progenitors (e.g., Saitoh et al. 2009; Iono et al. 2013; Saito et al. 2015; Kaneko et al. 2018).

In order to improve our understanding of the nonlinear response of gas during a collision, we require high-quality millimeter/submillimeter molecular line data that can trace the distribution and kinematics of cold molecular gas, the reservoir for future star formation. For nearby galaxies, low-J ^{12}CO, ^{13}CO, and C^{18}O lines ($n \simeq 10^2$–10^3 cm^{-3}) are usually employed to trace the total column density and the response of H$_2$ gas to violent merger events. The optically thin ^{13}CO and C^{18}O lines are rather important to constrain the physical properties of the diffuse molecular interstellar medium (ISM).

The gas-rich nearby interacting galaxy NGC 3110 ($D_{\rm L} = 69.4$ Mpc; $1'' = 325$ pc), which is classified as a nearby luminous IR galaxy (LIRG; $L_{\rm IR} = 10^{11.1} L_\odot$; Armus et al. 2009), is one of the best targets to study starbursts in early-stage interactions (Figure 1) because it is unique and because
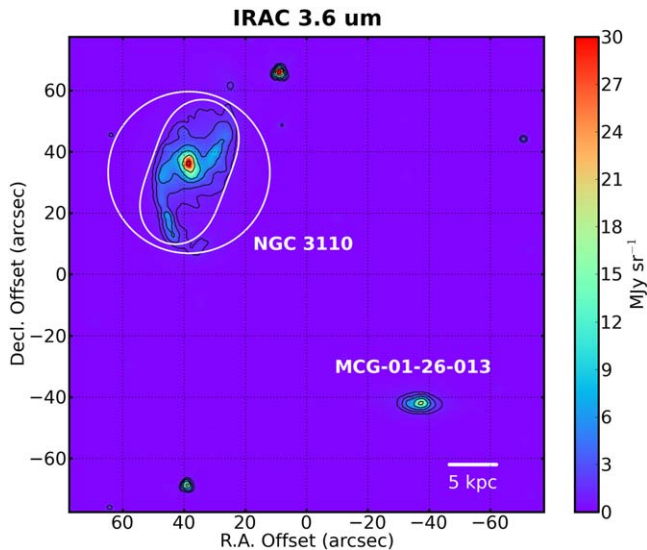
Figure 1. The IRAC 3.6 μm color image of NGC 3110. The circle and ellipse show the typical field of view of Band 3 and Band 6 observations, respectively. The companion galaxy MCG-01-26-013 can be seen below and to the right of NGC 3110.

rich multiwavelength observations are available and detailed simulations have reproduced its interacting nature in the literature (e.g., Espada et al. 2018). It consists of a central bar-like north–south elongation and a pair of asymmetric arms extending from the center, which are considered to be due to the tidal interaction with the companion galaxy MCG-01-26-013 located ~ 38 kpc southwest from the center of NGC 3110 (Espada et al. 2018). A recent near-IR survey (Randriamanakoto et al. 2013; Randriamanakoto 2015; Randriamanakoto & Väisänen 2017) reported the detection of more than 280 super star cluster (SSC) candidates across the disk, implying that NGC 3110 is one of the SSC-richest LIRGs in the low-redshift Universe. These SSCs, gravitationaly bound objects, are young and massive star clusters that are likely to form in strong starbursts and during galaxy–galaxy merging process (e.g., Whitmore et al. 1999; Randriamanakoto et al. 2019). Given its uniqueness and active star formation, studying NGC 3110 can provide valuable information for understanding how starbursts are triggered in early-stage mergers.

Another unique feature of this galaxy is the bright Hα blob at the southern edge of the southern tidal arm (Hattori et al. 2004). Espada et al. (2018) mapped ^{12}CO(2–1) with $\sim$1 kpc spatial resolution, and found an asymmetric gas distribution with a strong concentration around the nucleus that coincides with the Hα structures. They found that the average star formation efficiency (SFE) in the spiral arms is $\sim$0.5 dex higher than that in the circumnuclear region, implying that off-centered starbursts are triggered in early stages of the merger. They also carried out hydrodynamical minor merger simulations in order to reproduce the morphological characteristics (e.g., rotation curve) seen in their ^{12}CO(2–1) map and Hα map. They concluded that the prominent asymmetric two-armed structures in NGC 3110 is formed at $\sim$150 Myr after the closest approach, and the system is experiencing one of the highest star formation rate (SFR) episodes as a result of the flyby interaction with the minor companion galaxy.

Most previous extragalactic molecular gas studies that included NGC 3110 assumed a single ^{12}CO luminosity to H$_2$ gas mass conversion factor (α_{CO}), which is likely to vary

spatially among and within galaxies (Bolatto et al. 2013; Sandstrom et al. 2013), to derive the H$_2$ gas mass surface density and some relevant quantities such as the SFE. In order to better understand the missing properties of molecular gas, including α_{CO}, and the relation to star formation in merging galaxies, we have conducted multi-CO ALMA observations toward NGC 3110.

This paper is organized as follows: the ALMA observations, the data reduction, and the photometry method are summarized in Section 2, and the results are briefly summarized in Section 3. We describe how we derive the physical properties, e.g., H$_2$ gas mass, kinetic temperature, extinction-corrected SFR, and SSC number density, in Section 4. We discuss the star formation properties of NGC 3110 and their relation to the interaction event using the derived quantities (Section 5), and then summarize and conclude this paper in Section 6. We have adopted $H_0 = 70$ km s^{-1} Mpc^{-1}, $\Omega_m = 0.3$, and $\Omega_\Delta = 0.7$ throughout this paper.

2. Observations and Data Reduction

2.1. ALMA Observations

Observations of ^{12}CO and its isotopologs toward NGC 3110 were carried out during the ALMA cycle 2 period (ID: 2013.1.01172.S). We set four spectral setups whose upper sidebands were tuned to ^{12}CO or ^{13}CO. The main targeted lines are the $J = 1$–0 (Band 3) and 2–1 (Band 6) transitions of ^{12}CO, ^{13}CO, and C^{18}O. All data were obtained during 2014–2015. The single-sideband system temperature at Band 3 and Band 6 is 40–155 K and 65–135 K, respectively. The assigned antenna configurations for the Band 3 and Band 6 observations had 29–41 and 35–38 12 m antennas with a projected baseline length between 15–558 m and 15–348 m, respectively. Each tuning had four spectral windows (spws) to cover both sidebands. All spws had a bandwidth of 1.875 GHz with 7.812 MHz resolution. We used three pointings to cover all gaseous structures found in the ^{12}CO(2–1) image taken by the Submillimeter Array (Espada et al. 2010, 2018), although one pointing is enough for the Band 3 observations. All observation setups are summarized in Table 1.

2.2. Data Reduction

Data calibration and imaging were made using the Common Astronomy Software Applications package (CASA) version 4.2.2 (McMullin et al. 2007). When we reconstructed a ^{12}CO(2–1) image cube using the visibility data delivered from the observatory, we saw periodical linear patterns along one direction that were different from thermal noise structure. Thus, we carefully checked the visibility data and then flagged some data points whose amplitude deviated from the average value around a given baseline length. This additional flagging, as a result, suppressed the periodic patterns. We adopt this flagging reduction scheme for all ALMA data sets shown in this paper.

Images were reconstructed with the natural uv (robustness parameter = 2.0) weighting and a velocity resolution of 20 or 40 km s^{-1} depending on the achieved signal-to-noise ratio (S/N) of the targeted lines. Continuum emission was subtracted in the uv domain by fitting the line-free channels in the upper and lower sideband with a first-order polynomial function. The line-free channels were used to make a continuum image using the multifrequency synthesis method. We used the CASA task tclean in multiscale mode to make use of the multiscale

Table 1
Log of ALMA Observations

| Band | UT Date | Configuration | | | T_{sys} | Spectral Window | | t_{integ} | Calibrator | | |
		FoV ($''$)	N_{ant}	$L_{baseline}$ (m)	(K)	USB (GHz)	LSB (GHz)	(min.)	Flux	Bandpass	Phase
B3	2014 Jun. 28	57.2	29	19–639	40–70	107.529	95.669	26.6	Ceres	J1058+0133	J1008+0621
B3	2015 Mar. 9	54.7	30	15–328	55–155	112.487	100.414	28.1	Ganymede	J1058+0133	J1011-0423
B3	2015 May. 16	54.7	41	21–558	40–100	112.480	100.406	23.0	J1058+015	J1058+0133	J1011-0423
B6	2014 Dec. 8	28.6	35	15–349	65–115	229.970	215.805	17.5×3	Ganymede	J1037-2934	J1011-0423
B6	2014 Dec. 10	27.3	38	15–349	65–135	242.443	227.702	14.7×3	Callisto	J1037-2934	J1011-0423

Note. Column 3–5: Field of view, N_{ant}, and $L_{baseline}$ are the FWHM of the ALMA primary beam, number of 12 m antennas, and projected baseline length of the assigned configuration, respectively. Column 7–8: Central frequency of the two continuous spws in the upper and lower sidebands (USB and LSB). Column 9: Total integration time on NGC 3110. The Band 6 observations have three pointing fields due to the small field of view. Column 10–12: Assigned calibrators.

Table 2
Line and Imaging Properties

Line	ν_{obs} (GHz)	E_u/k (K)	uv-weight	Beam Size (P.A.) ($''$ (°))	V_{ch} (km s^{-1})	σ_{ch} (mJy beam^{-1})	$S_{line}\Delta v$ (Jy km s^{-1})
^{12}CO ($J=1-0$)	113.360	5.5	natural	1.81×1.43 (−82)	20	1.2	303.34 ± 1.91
^{12}CO ($J=2-1$)	226.716	16.6	natural	1.68×0.93 (+74)	20	1.2	854.84 ± 1.83
^{13}CO ($J=1-0$)	108.374	5.3	natural	1.16×1.14 (−32)	20	1.1	10.08 ± 0.69
^{13}CO ($J=2-1$)	216.744	15.9	natural	1.59×0.93 (+80)	20	0.7	38.01 ± 0.57
C^{18}O ($J=2-1$)	215.920	15.8	natural	1.59×0.93 (+80)	40	0.4	7.59 ± 0.25

Note. Column 6: Velocity resolution of the datacube. Column 7: Noise rms per channel per pixel in the data that have a velocity resolution of Δv. Column 8: Total integrated intensity. All the measurements were made after convolving the synthesized beam to $2''0$. We only consider the statistical error here.

CLEAN deconvolution algorithm (Cornwell 2008). All imaging properties for the detected molecular lines, including sensitivity and beam size, are listed in Table 2. Throughout this paper, we adopt typical systematic errors on the absolute flux calibration of 5% and 10% for the Band 3 and Band 6 data, respectively (Lundgren 2013).

Before making line intensity ratio maps, we flagged the uv range below $10 k\lambda$, so that the maximum recoverable scale (MRS) is the same in each ALMA image. The MRS definition we used in this paper is

$$\text{MRS} \approx 0.6 \frac{\lambda_{obs}}{L_{min}}, \qquad (1)$$

where λ_{obs} is the observed wavelength and L_{min} is the minimum projected baseline length (Lundgren 2013). The minimum uv distance is determined by the configuration of the ^{12}CO(2–1) observations. Since the truncated uv range at $10 k\lambda$ corresponds to the MRS of $\sim 10''7$ (3.5 kpc), we do not consider the missing flux effect on structures smaller than $10''7$. However, we caution that our ^{12}CO(1–0) data miss some extended emission (recovered flux = 77% ± 15%) compared to single-dish measurements (395 ± 79 Jy km s^{-1}; Sanders et al. 1991), which may affect our measurements on $3''0$ apertures, although fainter line data tend to be less affected. The aperture size is smaller than the MRS (described in Section 2.4). We made all maps and flux measurements after correcting for the primary beam attenuation. Then, we convolved all the ALMA line and continuum maps to $2''0$ resolution. We note that we used the original (i.e., untruncated) data for the gas mass measurement in this paper, although for all works requiring any line ratio, we used the truncated data.

After imaging, we created moment maps following the steps described here: (1) clip the ^{12}CO(1–0) datacube at 3σ (see Table 2), (2) convert the clipped cube into a 1/0 mask, (3) expand the mask by convolving by $2''0$ beam, and (4) collapse the data cubes after applying the expanded mask with 2.5σ clipping for the ^{12}CO data and 1.5σ for the other fainter data. This procedure allows us to include faint structures neighboring strong structures, and to exclude patchy faint structures that are likely artifacts.

2.3. Ancillary Data

In addition to the ALMA data, we use the Hα map obtained with Okayama Astrophysical Observatory (OAO) 188 cm telescope. The observations and data reduction are described in detail in Hattori et al. (2004). The reported spatial resolution is $1''35$, which is similar to the ALMA resolution. We also download the 1.4 GHz radio continuum map taken by Karl G. Jansky Very Large Array (VLA) from the VLA Data Archive.[15] These maps are used to construct an extinction-corrected SFR map (see Section 4). Furthermore, we use a high-quality K-band map obtained by Very Large Telescope (VLT; see Randriamanakoto et al. 2013 for details of the data), which provides the spatial distribution of SSCs.

2.4. Nyquist-sampled Aperture Photometry

In order to decrease the number of correlated data points and to unify the flux measurement method among images taken with different telescopes, a hexagonal Nyquist sampling (aperture diameter = $3''0$, aperture separation = $1''5$) was performed on all data taken by ALMA and complementary data from the OAO (Hα), VLT (K band), and VLA (radio

---

[15] https://archive.nrao.edu/archive

continuum) observations. In addition, the hexagonal gridding is one of the popular ways to analyze spatially resolved extragalactic systems (e.g., Sandstrom et al. 2013; den Brok et al. 2021). The Nyquist-sampled data points with flux stronger than 3σ will be used to derive physical parameters (Section 4) and to reconstruct physical parameter images.

We converted the observed integrated line flux density, $S\Delta v$ (Jy beam^{-1} km s^{-1}), into integrated line intensity, I (K km s^{-1}) using the conversion factor, β,

$$\frac{\beta}{\text{Jy beam}^{-1}\text{ K}^{-1}} = 1.222 \times 10^6 \left(\frac{\theta_{\text{maj}}\theta_{\text{min}}}{\text{arcsec}^2}\right)^{-2} \left(\frac{\nu_{\text{obs}}}{\text{GHz}}\right)^{-2}, \quad (2)$$

where θ_{maj} and θ_{min} are the FWHM sizes in the major and minor axis of the synthesized beam, respectively, and ν_{obs} is the observed frequency.

The integrated line intensity per aperture, I_{area}, was calculated by

$$\frac{I_{\text{area}}}{\text{K km s}^{-1}} = \frac{\sum_i^{N_{\text{px,area}}} I_{\text{px,i}}}{N_{\text{px,area}}}, \quad (3)$$

where $I_{\text{px,i}}$ is the integrated line intensity at the ith pixel (K km s^{-1}), $N_{\text{px,area}}$ is the number of pixels within the $3''0$ aperture. $I_{\text{px,i}}$ is same as $\beta(S\Delta v)_{\text{px,i}}$, where $(S\Delta v)_{\text{px,i}}$ is the observed line flux density at the ith pixel in Jy beam^{-1} km s^{-1} unit. When calculating the ALMA and VLA continuum brightness temperatures per apertures, one just needs to replace I_{area}, $I_{\text{px,i}}$, $(S\Delta v)_{\text{px,i}}$ with $T_{\text{b,area}}$ (K), $T_{\text{b,px,i}}$ (K), $(S_{\nu_{\text{obs}}})_{\text{px,i}}$ (Jy beam^{-1}), respectively.

The statistical noise (i.e., sensitivity) per aperture, $\sigma_{\text{stat}}(I_{\text{area}})$, was calculated by the following equation (e.g., Hainline et al. 2004):

$$\frac{\sigma_{\text{stat}}(I_{\text{area}})}{\text{K km s}^{-1}} = \beta\sigma_{\text{ch}} V_{\text{ch}} \sqrt{N_{\text{ch}}}, \quad (4)$$

where σ_{ch} is the median single-channel rms per pixel (Jy beam^{-1}), V_{ch} is the velocity width of a channel, and N_{ch} is the number of channels over which we integrated. For the continuum data, we used

$$\frac{\sigma_{\text{stat}}(T_{\text{b,area}})}{\text{K}} = \beta\sigma_{\text{rms}}, \quad (5)$$

where σ_{rms} is the median rms per pixel.

When we consider the systematic error of the absolute flux calibration, σ_{sys}, as well as σ_{stat}, we combined both errors using the equation

$$\sigma_{\text{tot}} = \sqrt{\sigma_{\text{stat}}^2 + \sigma_{\text{sys}}^2}, \quad (6)$$

where we assume that both errors are independent. Note that all the maps shown in this paper are clipped based on σ_{stat}, whereas the error bars in all the plots are calculated based on σ_{tot}.

Hereafter, integrated flux density and integrated intensity of a certain line, for example ^{12}CO(1–0), will be written as $S_{\text{CO(1–0)}}\Delta v$ and $I_{\text{CO(1–0)}}$, respectively.

The line luminosity per aperture can be calculated from

$$\frac{L'_{\text{line}}}{\text{K km s}^{-1}\text{ pc}^2} = 3.25 \times 10^7 S_{\text{line}}\Delta v\, \nu_{\text{obs}}^{-2} D_{\text{L}}^2 (1+z)^{-3}, \quad (7)$$

where D_{L} is the luminosity distance (=69.4 Mpc), and z is the redshift (Solomon & Vanden Bout 2005). In this paper, the ^{12}CO(1–0) luminosity is used to calculate α_{CO}.

3. Results

Figure 2 shows the integrated intensity and intensity-weighted velocity maps of the ^{12}CO, ^{13}CO, and C^{18}O lines. We confirm a bright central north–south bar-like elongated structure, a northern shorter arm, and a southern longer arm in all the ^{12}CO, ^{13}CO, and C^{18}O lines, which were previously identified by Submillimeter Array observations (Espada et al. 2010, 2018). Moreover, diffuse flocculent components filling in the inter-arm regions are also identified in ^{12}CO, which coincide with the diffuse, clumpy Hα components (Hattori et al. 2004). The ^{12}CO velocity fields show a rotating disk-like signature with an S-shaped noncircular motion, indicating the presence of inflow motions and/or a warped disk, as seen in other galaxies (Espada et al. 2012; Saito et al. 2017).

Both the ^{13}CO and C^{18}O images coincide with strong features in the ^{12}CO images. Similar to the asymmetric spiral structures seen in the Hα, SSC, and CO maps (Espada et al. 2018), we found a remarkably thin, long southern arm and an isolated blob in the south part of the northern arm in these isotopolog lines. We note that C^{18}O(1–0), which is also covered by one of our tunings, was marginally detected only around the very center, and thus we do not use this line in this paper.

3.1. Band 3 and Band 6 Continuum Emission

We detected 2.9 mm (Band 3) and 1.3 mm (Band 6) continuum emission toward the central bar-like structure and some parts of the arms in NGC 3110 (Figure 3). For normal star-forming galaxies without a strong signature of an active galactic nucleus (AGN), the 1.3 mm continuum emission is mostly dominated by thermal dust emission, whereas thermal free–free emission dominates the 2.9 mm continuum emission with a minor contribution from nonthermal synchrotron emission (e.g., Condon 1992; Saito et al. 2016). We discuss the physical origin of the emission based on the spectral index in Section 4.

3.2. Line Intensity Ratios

Here we present line ratios made from some combinations of the observed CO lines, which are sensitive to galactic-scale physical properties of molecular gas ISM. The notations of the intensity ratios are defined as

$$^X R_{J_u J_l / J'^u J'^l} \equiv \frac{I_{X(J_u - J_l)}}{I_{X(J'^u - J'^l)}}$$

$$^{X/Y} R_{J_u J_l} \equiv \frac{I_{X(J_u - J_l)}}{I_{Y(J_u - J_l)}} \quad (8)$$

,where the first indicates the ratio of different transitions for the main molecule or its isotopolog, and the second indicates the ratio of different isotopes for the same line transition. The spatial distributions of the $J = 2$–$1/J = 1$–0 ratios, $^{12}R_{21/10}$ and $^{13}R_{21/10}$, are shown in the top panel of Figure 4. $^{12}R_{21/10}$ shows a smooth distribution over the entire arms and bar-like elongation ($\sim$0.8 on average). $^{13}R_{21/10}$ peaks at the center
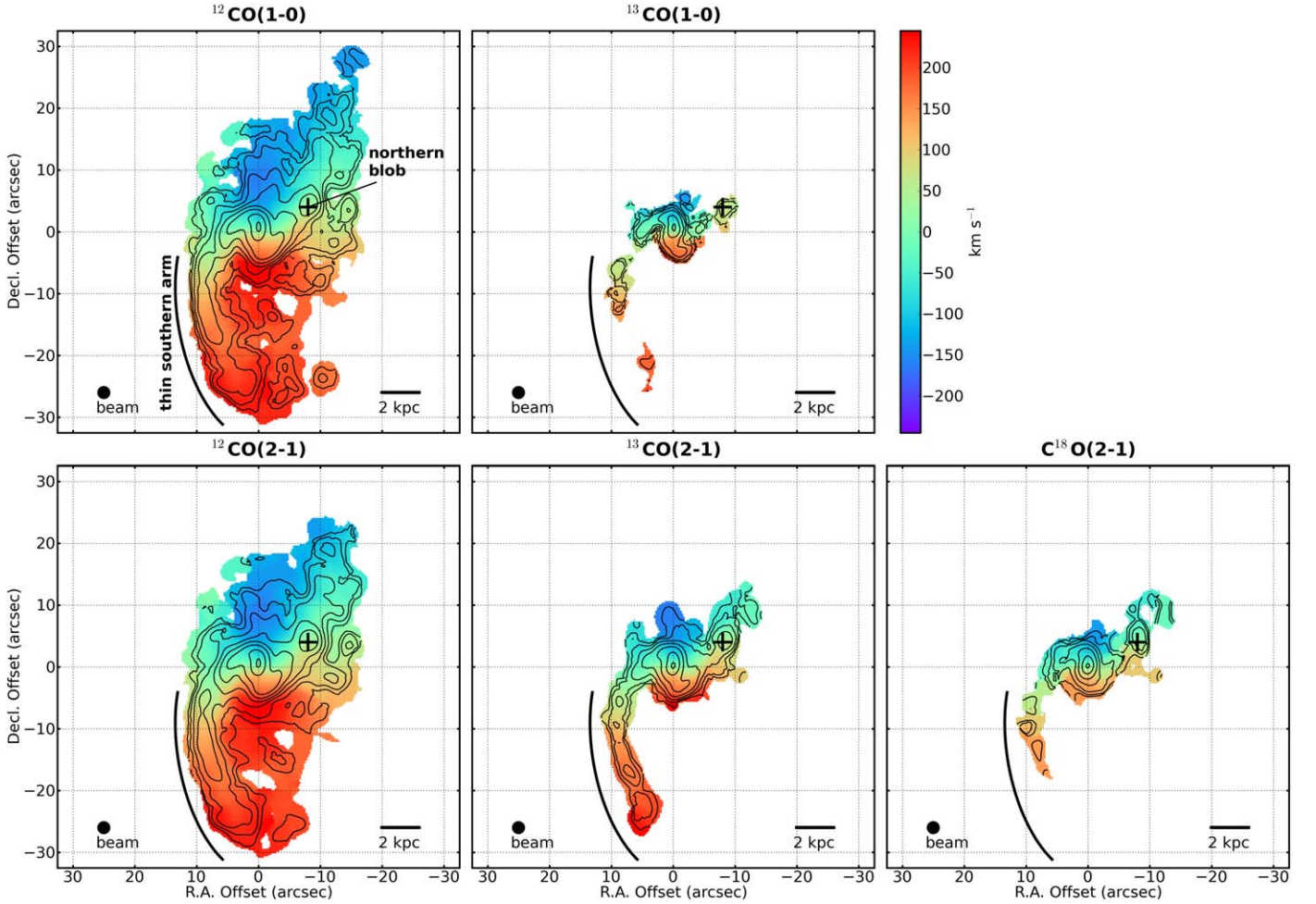
Figure 2. (top left) $^{12}CO(1–0)$ integrated intensity contours overlaid on $^{12}CO(1–0)$ intensity-weighted velocity field color image. The contours are $21.6 \times (0.01, 0.02, 0.04, 0.08, 0.16, 0.32, 0.64,$ and $0.96)$ Jy beam^{-1} km s^{-1}. The center position of this image is $(\alpha, \delta)_{J2000} = (10^h04^m02^s.090, -6^d28^m29^s.604)$. (top middle) $^{12}CO(2–1)$ image. The contours are $67.1 \times (0.01, 0.02, 0.04, 0.08, 0.16, 0.32, 0.64,$ and $0.96)$ Jy beam^{-1} km s^{-1}. (top right) $^{13}CO(1–0)$ image. The contours are $1.85 \times (0.02, 0.04, 0.08, 0.16, 0.32, 0.64,$ and $0.96)$ Jy beam^{-1} km s^{-1}. (bottom left) $^{13}CO(2–1)$ image. The contours are $5.70 \times (0.02, 0.04, 0.08, 0.16, 0.32, 0.64,$ and $0.96)$ Jy beam^{-1} km s^{-1}. (bottom right) $C^{18}O(2–1)$ image. The contours are $2.16 \times (0.02, 0.04, 0.08, 0.16, 0.32, 0.64,$ and $0.96)$ Jy beam^{-1} km s^{-1}.
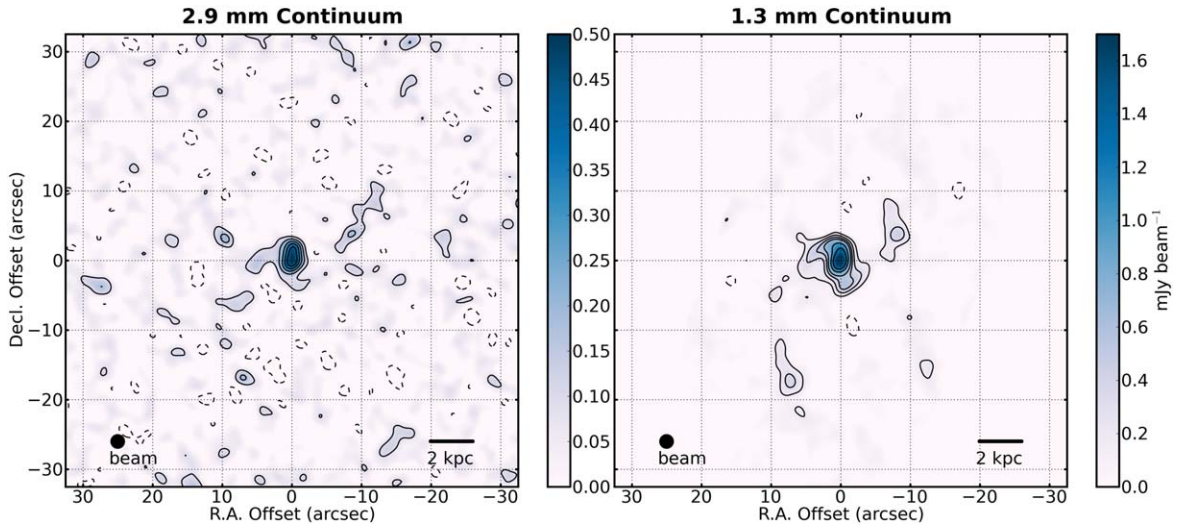
Figure 3. (top) The 2.9 mm continuum image of NGC 3110. The contours are -2.0, 2.0, 4.0, 6.0, 8.0, and 10.0σ. 1σ corresponds to 41.8 μJy beam^{-1}. The center position of this image is the same as in Figure 2. (bottom) The 1.3 mm continuum image. The contours are $-2.5, 2.5, 5.0, 7.5, 10.0, 15.0,$ and 20.0σ. 1σ corresponds to 62.7 μJy beam^{-1}.

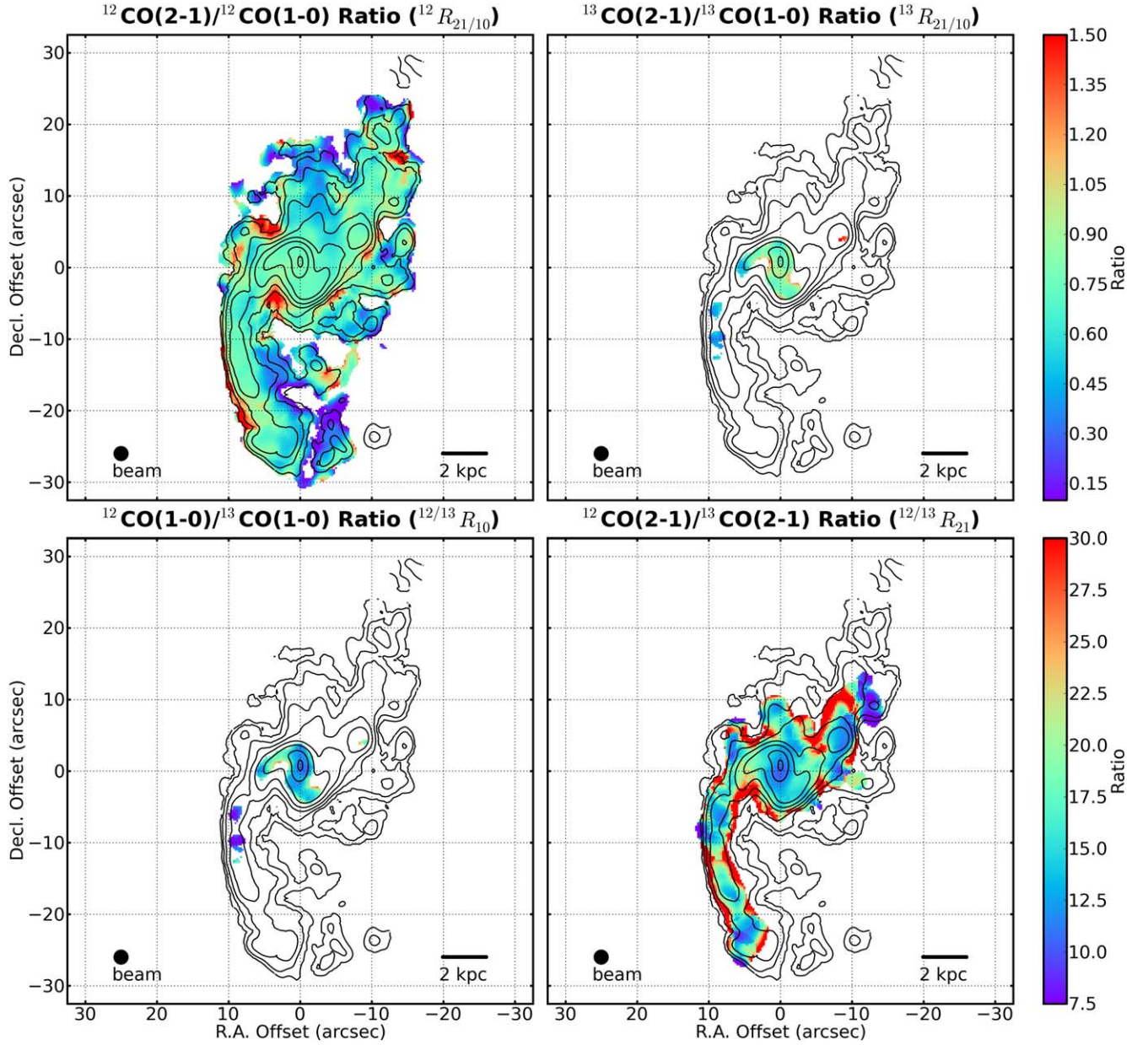**Figure 4.** (top) ^{12}CO(2–1)/^{12}CO(1–0) and ^{13}CO(2–1)/^{13}CO(1–0) intensity ratio images of NGC 3110. The contours show the CO (1–0) integrated intensity image. The center position of this image is the same as in Figure 2. (bottom) Same as the top panel, but for the ^{12}CO(1–0)/^{13}CO(1–0) and ^{12}CO(2–1)/^{13}CO(2–1) intensity ratios.

($\sim$1.0), with lower values at the ends of the elongation ($\sim$0.7) and the southern arm ($\sim$0.4). The spatial distributions of the ^{12}CO/^{13}CO ratios, $^{12/13}R_{10}$ and $^{12/13}R_{21}$, are shown in the bottom panel of Figure 4. Unlike the $^{12}R_{21/10}$ and $^{13}R_{21/10}$ distributions, $^{12/13}R_{21}$ shows a lower value ($\sim$10) at the nuclear region, higher values ($\sim$30) toward $\sim$5″ east and west from the nucleus, and then lower values again at the tip of the southern arm (bottom panel of Figure 4). $^{12/13}R_{10}$ also shows a similar trend, although the low S/N is insufficient. These spatial variations can be clearly seen in the radial profiles in Figure 5.

4. Derivation of Physical Parameters

In this section, we describe how we derive α_{CO}, the spectral index between 1.3 mm and 2.9 mm, the extinction-corrected SFR, and the number density of SSC based on the data taken

by using the Nyquist-sampled 3″0 apertures. The derived parameters are visualized in Figure 6.

4.1. Non-LTE Calculation Using RADEX

We used the nonlocal thermodynamic equilibrium (non-LTE) radiative transfer code RADEX (van der Tak et al. 2007) and compared with the observed line ratios. We derived the physical conditions of molecular gas, assuming a single-phase ISM (i.e., the gas physics can be represented by a single set of the excitation parameters), an expanding-sphere geometry ($dv = 100 \, \mathrm{km \, s^{-1}}$), a cosmic microwave background temperature ($T_{bg} = T_{CMB} = 2.73$ K), and [CO]/[H$_2$] ($= 3 \times 10^{-4}$) and [CO]/[^{13}CO] ($= 70$) abundances, which are same as those applied for the LTE calculation described later. The upper state energies and the Einstein coefficients were taken from the Leiden Atomic and Molecular Database (Schöier et al. 2005).
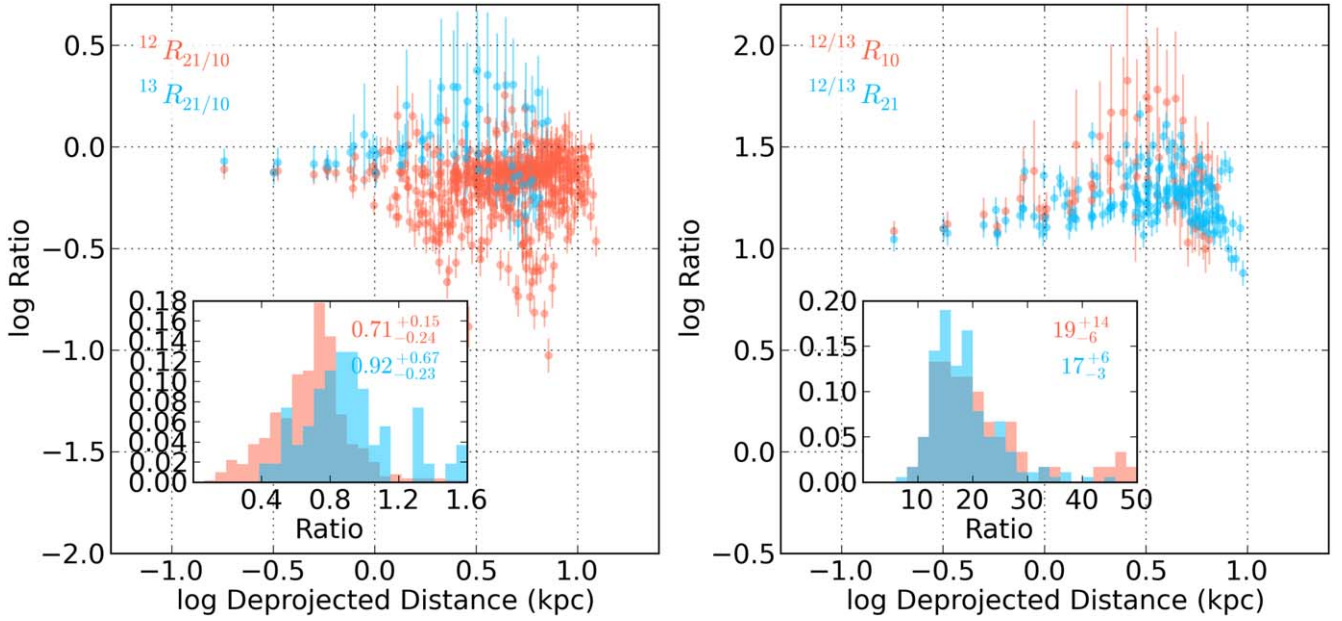
Figure 5. (left) The deprojected radial distribution of $^{12}R_{21/10}$ and $^{13}R_{21/10}$. Each data point is measured by the $3\rlap.{''}0$ ($\sim$1 kpc) aperture. We assumed a P.A. = 171° and an inclination = 65° (Espada et al. 2018). The inset shows the ratio distributions. The median values with the 16th and 84th widths are shown in the top right corner. (right) The deprojected radial distribution of $^{12/13}R_{10}$ and $^{12/13}R_{21}$.

We made model grids within the range of the gas kinetic temperature (T_{kin}) = 5–205 K, the gas volume density ($n_{\mathrm{H_2}}$) = $10^{2.0}$–$10^{7.0}$ cm^{-3}, and H$_2$ gas column densities ($N_{\mathrm{H_2}}$) = $10^{22.0}$–$10^{22.5}$ cm^{-2}. After deriving best-fit values at each aperture via a χ^2 minimization, we made Nyquist-sampled T_{kin} and $n_{\mathrm{H_2}}$ images as shown in the top left and top center panels of Figure 6. We regard the 90% confidence area in the parameter space as the uncertainty of the derived T_{kin} and $n_{\mathrm{H_2}}$ following the standard way (e.g., Sliwa et al. 2014).

4.2. The CO-to-H₂ Conversion Factor

For extragalactic objects, the ^{12}CO(1–0) and ^{12}CO(2–1) lines are popular and well-calibrated H$_2$ gas mass tracers (see Bolatto et al. 2013, for a review). This is mainly because the sensitivity of the radio instruments is not enough to detect optically thin low-density molecular gas tracers. Recent high-sensitivity interferometric studies provided several ways to calibrate α_{CO}: the gas mass measured by kinematics (i.e., dynamical mass; e.g., Downes & Solomon 1998), the gas-to-dust ratio (e.g., Sandstrom et al. 2013), and a radiative transfer analysis with multiple molecular lines (e.g., Sliwa et al. 2017).

In this paper, we estimate the H$_2$ gas mass ($M_{\mathrm{H_2}}$) with two different methods and then compare with $L'_{\mathrm{CO(1-0)}}$.

4.2.1. LTE Mass Derivation

One reliable way to estimate $M_{\mathrm{H_2}}$ is to use optically thin molecular gas tracers. In this paper, we observed two transitions of ^{13}CO, which are usually thought to be optically thin, in order to solve the radiative transfer equation. Multiple transition data allow us to directly estimate the excitation temperature (T_{ex}) and the column density of the molecule assuming LTE, resulting in accurate molecular gas mass (M_{LTE}). Since the number of apertures with a detection of both ^{13}CO transitions higher than 3σ is lower than 20 (mostly in the nuclear region and the southern arm), we first determine the typical T_{ex} for these $\lesssim$20 apertures and then assume a single T_{ex}

in order to derive the column density for many more apertures. Here we employ the following equation:

$$\frac{I_{^{13}\mathrm{CO}}}{\mathrm{K\ km\ s^{-1}}} = \frac{8\pi S \mu_0^2 \nu N_{^{13}\mathrm{CO}}}{3kQ(T_{\mathrm{rot}})}\left\{1 - \frac{\exp(h\nu/kT_{\mathrm{rot}}) - 1}{\exp(h\nu/kT_{\mathrm{bg}}) - 1}\right\} \times \exp\left(-\frac{E_{\mathrm{u}}}{kT_{\mathrm{rot}}}\right),\qquad(9)$$

where S, μ_0, ν, $N_{^{13}\mathrm{CO}}$, k, Q(T_{rot}), T_{rot}, h, T_{bg}, and E_{u} are the line strength, dipole moment, transition frequency, total column density of ^{13}CO, the Boltzmann constant, the partition function, rotation temperature, which is the same as T_{ex}, the Planck constant, the cosmic microwave background temperature, and the upper state energy, respectively (e.g., Goldsmith & Langer 1999; Watanabe et al. 2014; Nakajima et al. 2018). We took the transition parameters necessary for calculating the equation from Splatalogue[16] and the Cologne Database for Molecular Spectroscopy (Müller et al. 2001, 2005).

The median and average T_{rot} are 15.1 K and 15.4 K, respectively. Thus we substituted $T_{\mathrm{rot}} = 15$ K for Equation (9) in order to estimate $N_{^{13}\mathrm{CO}}$ for all apertures with a ^{13}CO(2–1) detection. Then, M_{LTE} is derived by using the equation

$$\frac{M_{\mathrm{LTE}}}{M_\odot} = 1.36 \frac{N_{^{13}\mathrm{CO}}}{[^{13}\mathrm{CO}]/[\mathrm{H_2}]} m_{\mathrm{H_2}} A_{\mathrm{aperture}},\qquad(10)$$

where $m_{\mathrm{H_2}}$ is the mass of the hydrogen molecule, A_{aperture} is the area of the apertures, and $[^{13}\mathrm{CO}]/[\mathrm{H_2}]$ is the ^{13}CO abundance relative to H$_2$. Here we assumed $[^{13}\mathrm{CO}]/[\mathrm{H_2}] = 4.3 \times 10^{-6}$, which is similar to the standard value observed in Galactic warm, star-forming molecular clouds ($[^{12}\mathrm{CO}]/[^{13}\mathrm{CO}] = 70$, $[^{12}\mathrm{CO}]/[\mathrm{H_2}] = 3.0 \times 10^{-4}$; e.g., Blake et al. 1987; Lacy et al. 1994). These are commonly used values in (U)LIRG studies (e.g., Sliwa et al. 2014). In order to accurately constrain the
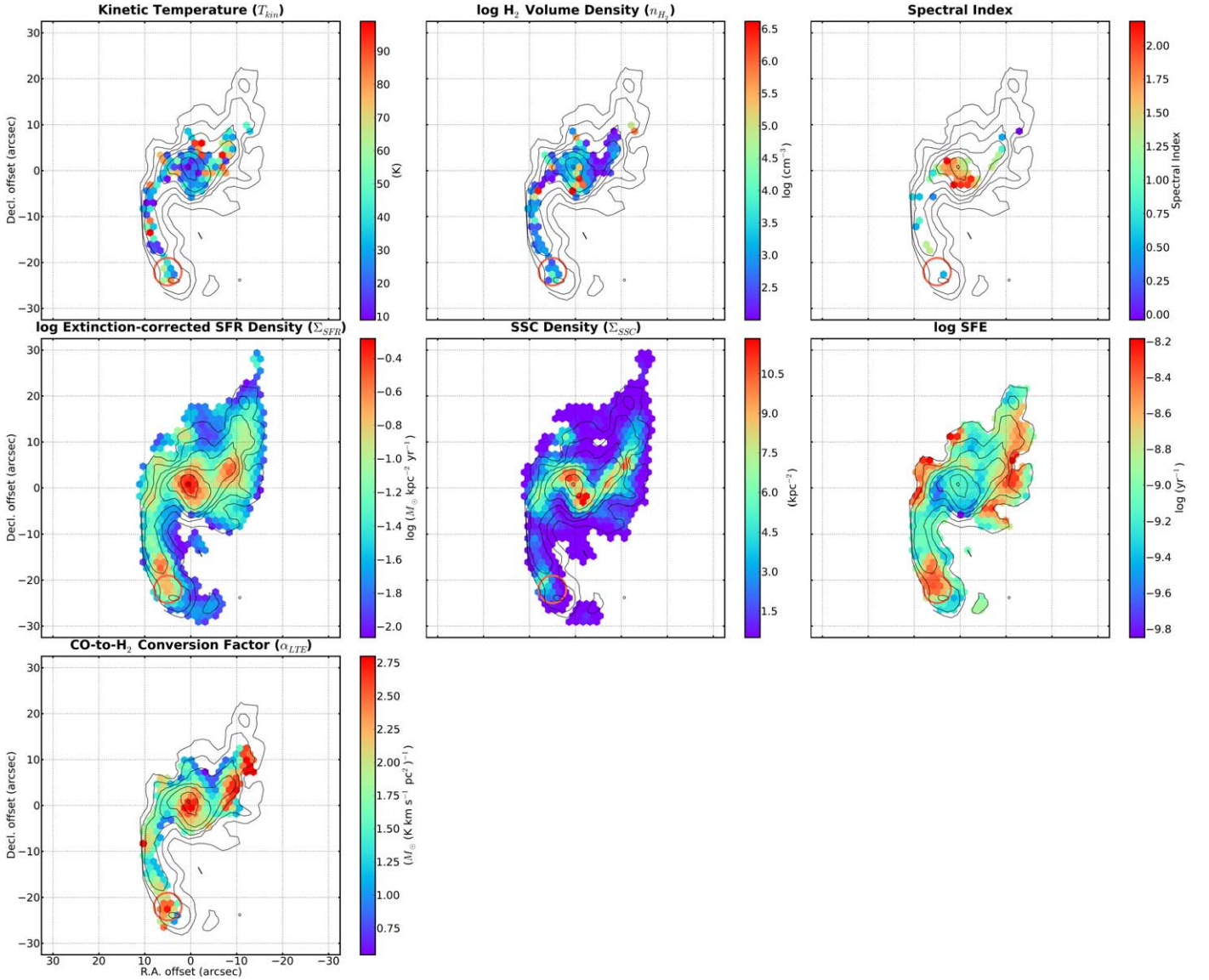
---

[16] http://www.cv.nrao.edu/php/splat/

Figure 6. (top left) The T_{kin} map (RADEX output) of NGC 3110 reconstructed from the 3″0 Nyquist-sampling analysis. The overlaid CO (1–0) integrated intensity contours are also reconstructed using the same sampling procedure. The red circle presents the approximate position of region A (see text). The center position of this image is the same as in Figure 2. (top center) The n_{H_2} map (RADEX output). (top right) The 2.9 mm to 1.3 mm spectral index map. (middle left) The extinction-corrected SFR surface density (Σ_{SFR}) map in logarithmic scale. (middle center) The SSC number density (Σ_{SSC}) map. (middle right) The SFE map in logarithmic scale. (bottom left) The CO-to-H_2 conversion factor (α_{CO}) map

abundance ratios in NGC 3110, we need a more sophisticated modeling and to increase the number of input maps and their quality. We multiply by 1.36 to account for the helium abundance relative to hydrogen. The derived 16th–50th–84th percentiles of α_{LTE} ($=M_{LTE}/L'_{CO(1-0)}$) are 1.30–1.69–2.21 $M_\odot$ (K km s^{-1} pc^2)$^{-1}$. The radial distribution of the derived α_{LTE} with $T_{rot} = 15$ K is shown as the red data points in the left panel of Figure 7. The spatial distribution is also shown in the bottom left panel of Figure 6.

Here we also derived α_{LTE} using T_{kin} ($=\alpha_{LTE}(T_{kin})$) derived in Section 4.1, instead of the fixed T_{rot}, based on the reasonable assumption that CO excitation is entirely dominated by collision with H_2. However, low-temperature and low-density gas is not usually in thermal equilibrium, so that we expect $T_{rot} < T_{kin}$. Thus, $\alpha_{LTE}(T_{kin})$ give the upper limit. Indeed, we confirmed that $\alpha_{LTE}(T_{kin})$ is about twice higher than $\alpha_{LTE}(T_{rot})$.

4.2.2. ISM Mass Derivation

One of the other methods for estimating the molecular gas mass is to use the Rayleigh–Jeans part of the thermal dust continuum emission, as described by Scoville et al. (2016). We derived molecular ISM masses (M_{ISM}) from the 1.3 mm dust continuum emission using the following equation:

$$\frac{M_{ISM}}{10^{10}M_\odot} = 1.78\, S_{\nu_{obs}}(1+z)^{-4.8}\left(\frac{\nu_{obs}}{\nu_{850\mu m}}\right)^{-3.8}\left(\frac{D_L}{\text{Gpc}}\right)^2$$

$$\times \left(\frac{6.7 \times 10^{19}}{\alpha_{850}}\right)\frac{\Gamma_0}{\Gamma_{RJ}}, \qquad (11)$$

where $S_{\nu_{obs}}$ is the observed continuum flux, $\nu_{850\mu m}$ is 353 GHz, ν_{obs} is the observed frequency ($=235$ GHz), α_{850} is the calibration
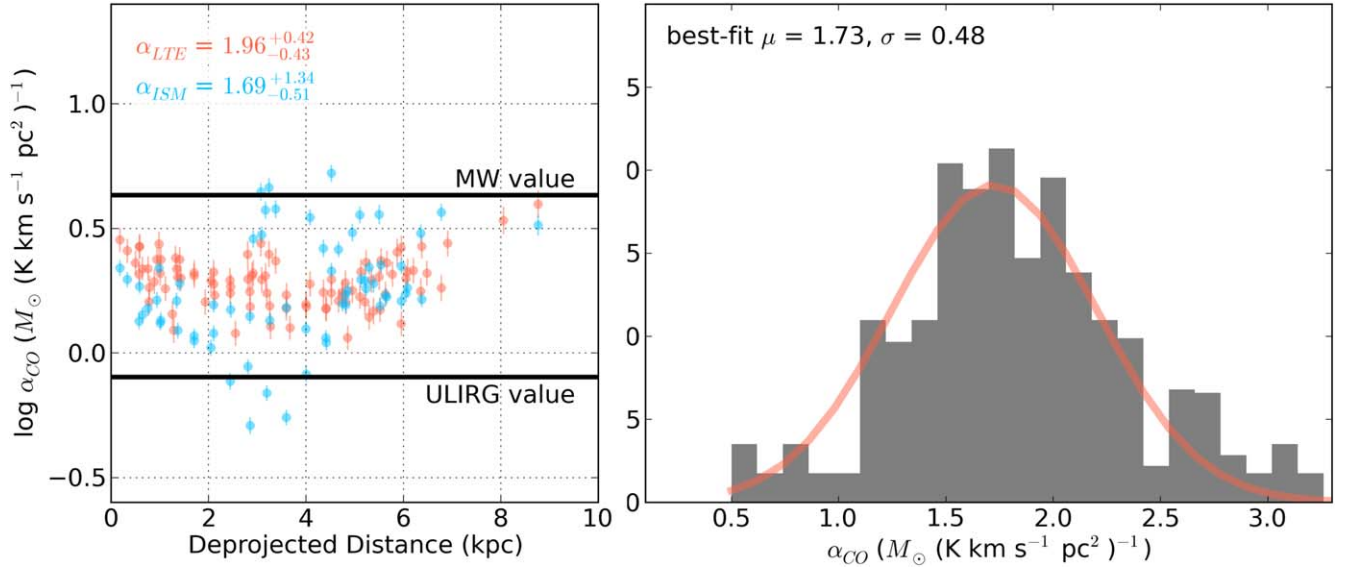
Figure 7. (left) Radial α_{CO} distributions based on LTE masses and ISM masses. The median values with the 16th and 84th widths are shown in the top right corner. The Galactic and (U)LIRG values are shown as solid black lines. (right) Distribution of the α_{CO}. The solid red line shows the best-fit Gaussian.

constant corresponding to 6.7×10^{19} erg s^{-1} Hz^{-1} $M_\odot^{-1}$ introduced by Scoville et al. (2016), and Γ_{RJ} and Γ_0 is given by

$$\Gamma_{RJ}(T_d, \nu_{obs}, z) = \frac{h\nu_{obs}(1+z)/kT_d}{e^{h\nu_{obs}(1+z)/kT_d} - 1} \qquad (12)$$

$$\Gamma_0 = \Gamma_{RJ}(T_d, \nu_{850\mu m}, 0), \qquad (13)$$

where T_d is the dust temperature. Here, we adopt $T_d = T_{rot}$ $(= 15$ K$)$ in order to estimate α_{ISM} $(= M_{ISM}/L'_{CO(1-0)})$, based on the empirical relation between the molecular gas condition and dust heating (Koda et al. 2020; Liu et al. 2021).

The radial α_{ISM} distributions as well as α_{LTE} are shown in the left panel of Figure 7. The derived 16th–50th–84th percentiles of α_{ISM} are 1.08–1.48–2.26 $M_\odot$ (K km s^{-1} pc^2)$^{-1}$.

4.2.3. Appropriate α_{CO} for NGC 3110

We found that the two methods show a nonmonotonic trend (i.e., decreasing, then increasing). However, we assume a flat α_{CO} hereafter, as the α_{CO} assumption (e.g., varying or constant) does not affect the discussion of this paper (see the Appendix). The assumed flat α_{CO} distribution is consistent with spatially resolved α_{CO} values for other nearby spirals (Sandstrom et al. 2013) and the LIRG NGC 1614 (Saito et al. 2017). Figure 7 (right) shows the histogram of $\alpha_{ISM}(T_{rot})$ with a best-fit Gaussian (peak = 1.73 and dispersion = 0.48). In this paper, we adopt a fixed α_{CO} of 1.7 $M_\odot$ (K km s^{-1} pc^2)$^{-1}$ when measuring gas masses. Note that this α_{CO} value is consistent with values derived for other (U)LIRGs (e.g., Sliwa et al. 2017).

The increasing α_{LTE} trend around the central kiloparsec of NGC 3110 is opposite to the trend found around the center of nearby galaxies (Sandstrom et al. 2013; Saito et al. 2017). We explain that this increasing trend is due to the assumed constant T_{rot}. According to Equation (9), twice higher T_{rot} results in $\lesssim 0.5$dex lower N_{13CO}. Thus, the α_{LTE} trend will be flattened or even inversed if we are able to measure T_{rot} at each aperture. Although one of our original motivations to observe multiple transitions is to study the temperature effect on the gas mass

measurements around the galaxy centers, the S/Ns of our ^{13}CO(1–0) map are insufficient to measure the spatial T_{rot} distribution.

4.3. Spectral Index: Two Thermal Components

The millimeter/submillimeter part of the spectral energy distribution of a star-forming galaxy is known to be dominated by nonthermal (synchrotron) and thermal (free–free and cold dust) emission (e.g., Condon 1992). The two thermal components in particular are more important in the higher frequency regime ($\gtrsim$100 GHz), because the steep negative spectral index of the nonthermal continuum ($\alpha \sim -0.8$) makes it weaker than the other two ($\alpha \sim -0.1$ and 2–4 for free–free and dust, respectively). Based on our Band 3 and Band 6 data, we can roughly study the continuum property using the following equation:

$$\alpha_{\nu_2}^{\nu_1} = \log_{\frac{\nu_1}{\nu_2}} \frac{S_{\nu_1}}{S_{\nu_2}} \qquad (14)$$

,where ν_i is the observed frequency, and S_{ν_i} is the observed flux at ν_i. The derived spectral index image is shown in the top right panel of Figure 6. We found that the central part of NGC 3110 is dominated by the steep dust emission, although the southern tip of the southern arm shows a relatively low spectral index ($\gtrsim 0.4$), implying a non-negligible contribution from the free–free emission (i.e., H II regions containing ionizing stars).

4.4. SFR Derivation and Extinction Correction

Here we calculate the other important physical parameter, the SFR based on previous Hα data taken by OAO (Hattori et al. 2004) and archival 1.4 GHz continuum.

In order to estimate the extinction-corrected Hα luminosity ($L(H_\alpha)_{corr}$), we used the prescription described by Kennicutt et al. (2009),

$$\frac{L(H_\alpha)_{corr}}{erg\ s^{-1}} = L(H_\alpha)_{obs} + 0.39 \times 10^{13} L(1.4\ GHz), \qquad (15)$$

where $L(H_\alpha)_{obs}$ is the observed Hα luminosity in erg s^{-1} unit, and $L(1.4GHz)$ is the observed 1.4 GHz radio continuum luminosity in erg s^{-1} Hz^{-1} unit. Then, we measure extinction-corrected SFR at each aperture using the following equation (see Kennicutt & Evans 2012 for a review):

$$\frac{\text{SFR}}{M_\odot \text{ yr}^{-1}} = \frac{L(H_\alpha)_{corr}}{10^{41.27}}. \quad (16)$$

The derived total SFR from the extinction-corrected Hα data (i.e., summed over all independent apertures) is $\sim 18 \, M_\odot$ yr^{-1} (middle left panel of Figure 6).

We caution that the employed extinction-correction prescription is based on the global measurements (see Kennicutt et al. 2009), and therefore our spatially resolved SFRs are uncertain. However, we confirmed that the measured total SFR is in agreement with values derived in the literature: U et al. (2012) derived $\sim 24 \, M_\odot$ yr^{-1} based on the IR spectral energy distribution, and Espada et al. (2018) derived 19.7 $M_\odot$ yr^{-1} and 21.2 $M_\odot$ yr^{-1} based on Hα+24 μm and 24 μm, respectively. In addition, the global trend seen in the Kennicutt–Schmidt (KS) relation (see the next section) is also consistent with the relation described in Espada et al. (2018) (although the scatter is larger in our KS relation, which is clearly seen in the data points with a deprojected distance from 3 to 6.5 kpc). After this double-checking, we decided to use this prescription in this paper. Constructing an accurate SFR map at high angular resolution comparable to the ALMA resolution is beyond the scope of this paper, but is a necessary step to further understand the star formation activities in NGC 3110.

4.5. Kennicutt–Schmidt Relation

We plot the ($\sim$1 kpc-scale) NGC 3110 data points on the KS Σ_{SFR} - Σ_{H_2} relation (Kennicutt 1998b), as shown in the top left panel of Figure 8. Note that if adopting variable α_{LTE}, the KS relation does not change qualitatively, and even the difference between the circumnuclear region and the arms becomes larger; i.e., the central part of this galaxy shows higher densities, and the SFE ($=\Sigma_{SFR}/\Sigma_{H_2}$) is high 7–8 kpc away from the nucleus. The SFE map using a fixed α_{CO} is shown in the middle right panel of Figure 6. The highest SFE can be found inside the red circle around the southern tip of the southern arm.

Comparing with similar resolution ($\sim$0.75 kpc) data for local noninteracting spiral galaxies (Bigiel et al. 2008), NGC 3110 shows comparable or higher Σ_{SFR} and Σ_{H_2} than spiral galaxies with the highest Σ_{SFR} ($\lesssim 1 \, M_\odot$ kpc^{-2} yr^{-1}) and Σ_{H_2} ($\lesssim 10^{2.5} \, M_\odot$ pc^{-2}), even though NGC 3110 is in an early stage of interaction. The SFEs of NGC 3110 range from 10^{-8} to 10^{-9} yr^{-1}, which is higher than that of spiral galaxies ($\sim 5 \times 10^{-10}$ yr^{-1}). Especially, at the southern tip of the southern arm (hereafter region A; shown as a red circle in Figure 6), the SFE is $\sim 10^{-8}$ yr^{-1}, which is about four times higher than the average SFE around the nuclear region. Our SFE values are consistent with previous SFE values (Espada et al. 2018) if we use the same α_{CO} as were used previously (i.e., 4.3 $M_\odot$ (K km s^{-1} pc^2)$^{-1}$ instead of 1.7 $M_\odot$ (K km s^{-1} pc^2)$^{-1}$).

We note that the prescriptions to derive the SFR are different in this study and in other papers introduced in this section: the far-ultraviolet and 24 μm were used in Bigiel et al. (2008), Hα and 24 μm were used in Espada et al. (2018), and Hα and radio continuum were used in this study. This introduces systematic

uncertainties in the absolute values, and thus hereafter, we focus on our own data.

5. Discussion

5.1. Star Formation at the Tip of the Southern Arm

The southern tip of the southern arm, region A, shows the highest SFE of the NGC 3110 data points, which is an unusual feature for spiral galaxies, which typically show the highest SFE around the center (Leroy et al. 2008). Here we try to characterize the physical properties of the highest SFE region.

One of the intriguing features seen in region A is the shallow spectral index between 1.3 mm and 2.9 mm. In the top right panel of Figure 8, we plot the SFE against the spectral index. The data points with the deprojected radius <3 kpc (yellow to red) tend to distribute around the spectral index $\sim$1–3, indicating dusty star formation in the central region of NGC 3110. In contrast to the center, the outer part, especially region A, shows a much lower spectral index ($\sim$0.5), implying that the 2.9 mm continuum from region A is likely to be significantly contaminated by the free–free emission from ionized gas by young massive stars (typical age $\lesssim$10 Myr; Kennicutt & Evans 2012). Such ionized gas can be also traced by Hα emission, which is used to derive the SFE. Considering that the IR continuum emission (3–1100 μm) is a good tracer of star formation with an age $\lesssim$100 Myr (Kennicutt & Evans 2012), the trend seen in the top right panel of Figure 8 tells us the dominant age of the star-forming regions. Thus, region A is likely to be an active and young star-forming region in the disk of NGC 3110, whereas the central part of NGC 3110 is a site of more dusty, long-continued star formation. We note that the discussion of the spectral index in region A is based on a single data point, as shown in the top right panel of Figure 8. Although the S/N is sufficient to safely conclude the relatively lower spectral index in region A, continuum observations with higher accuracy are required to better constrain the age differences.

We plot the SFE against Σ_{SSC} in the bottom panel of Figure 8, showing no clear correlation between them. However, the tendency is that the inner regions (i.e., redder points) show a relatively lower SFE ($\gtrsim 10^9$ yr^{-1}) but higher Σ_{SSC} ($\sim$10 kpc^{-2}). Since the typical age of SSCs is thought to be 10–100 Myr (Randriamanakoto 2015), the trend seen in the bottom panel of Figure 8 supports the idea that region A is a younger massive star-forming region compared with those around the center.

5.2. Early-stage Minor Merger as a Trigger of Wide-spread Star Formation

The relative age difference between the star-forming regions around the central region and region A is an important clue to understand the physical origin of the kiloparsec-scale star formation in the disk of NGC 3110. Numerical simulations suggested that tidal interaction between galaxies with a high mass ratio enhances both a long-lived $m = 2$ bar and transient asymmetric arms (Iono et al. 2004; Cox et al. 2008; Pettitt & Wadsley 2018). Espada et al. (2018) reproduced the morphological characteristics of NGC 3110 using hydrodynamical simulations, and found that NGC 3110 might be experiencing one of the highest SFR epochs during the merger history before coalescence. The typical SSC age is comparable to or shorter than the timescale of the merger-induced
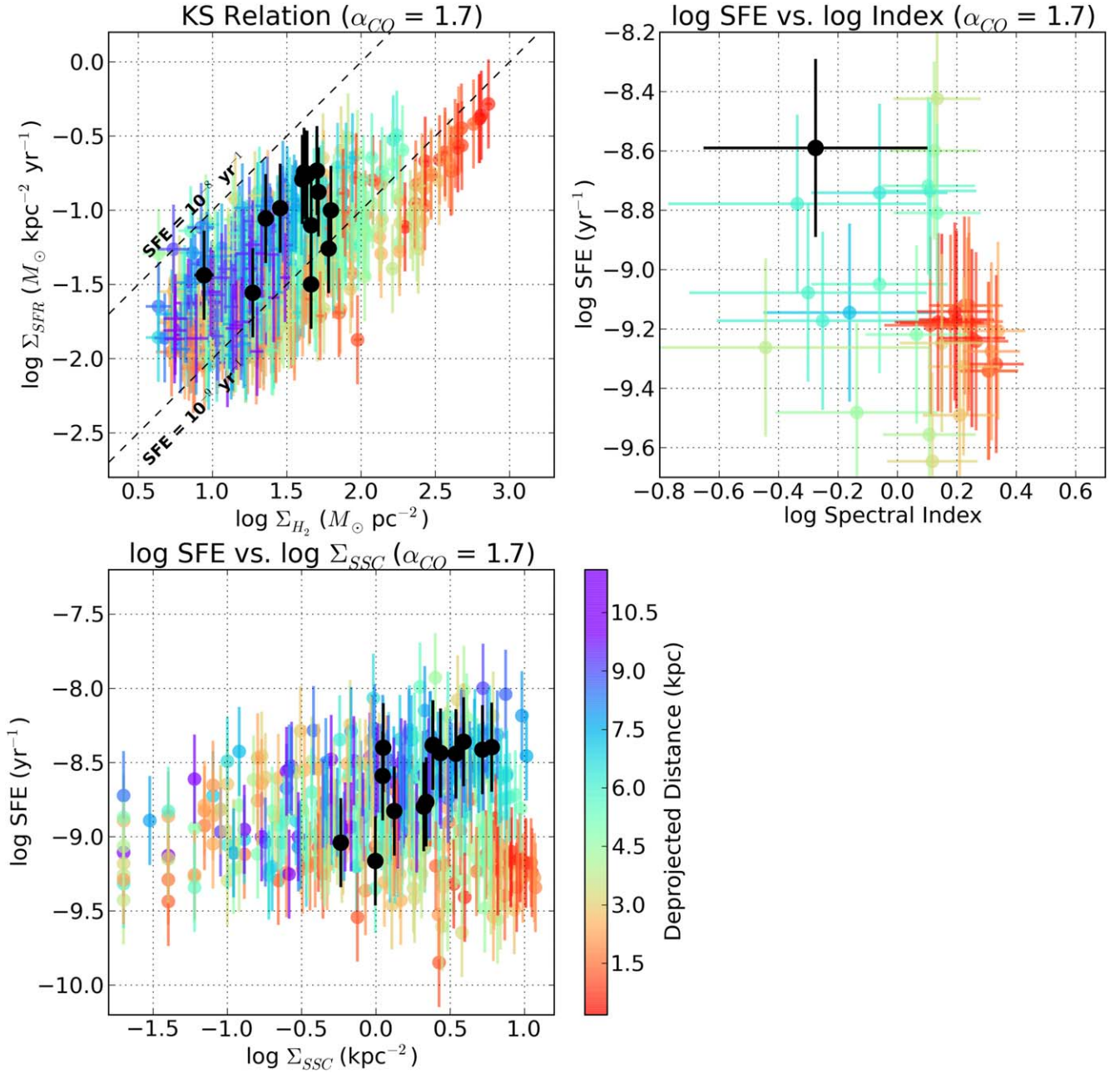
Figure 8. (top left) The 1 kpc scale KS relation of NGC 3110. The black data indicate measurements toward region A. The dashed lines show a constant SFE of 10^{-8} and 10^{-9} yr^{-1}. The color scale corresponds to the distance from the nucleus. (top right) SFE plotted against spectral index. (bottom) SFE plotted against $\Sigma_{\rm SSC}$.

asymmetric arms in NGC 3110 reproduced by this simulation, which is consistent with the picture that the star-forming region in region A is triggered by tidal interaction. The star-forming regions triggered in the tidally induced transient arms show clumpy structures in the simulations, as we saw in the CO isotope images of NGC 3110 (Figure 2). Based on these morphological similarities between NGC 3110 and numerical minor merger simulations, we suggest that the ongoing interaction with the smaller companion galaxy MCG-01-26-013 triggers an active, young star-forming region (SFE $\sim 10^{-8.2}$ yr^{-1}, $\Sigma_{\rm SFR} \sim 10^{-0.6} M_\odot$ kpc^{-2} yr^{-1}, $\Sigma_{\rm SSC} \sim 6.0$ kpc^{-2}) at the southern tip of the southern arm in NGC 3110. The elevated star-forming activities seen in the center of NGC 3110 might be due to merger-driven tidal torques leading to rapid, large-scale gas inflow.

6. Summary

We present $\sim 1\rlap{.}''0$ resolution ALMA Band 3 and Band 6 observations of the rotational transitions of CO and its isotopologs and continuum emission in the nearby interacting LIRG NGC 3110. NGC 3110 has asymmetric two-armed spirals and a bar-like structure, both of which are likely to be enhanced during the early-stage galaxy merger interaction, as suggested by previous molecular gas observations and numerical simulations (Espada et al. 2018; Pettit & Wadsley 2018). Combining our new ALMA data sets with previous Hα and 1.4 GHz continuum data, we find that the highest SFE region is located at the southern tip of the southern spiral arm (region A). Region A is characterized with (1) a lower spectral index between 1.3 mm and 2.9 mm ($\lesssim 0.5$), i.e., a dominant contribution from free–free emission, (2) a high number

density of super star clusters ($\Sigma_{SSC} \sim 6.0\,\mathrm{kpc}^{-2}$), and (3) relatively active star formation (SFE $\sim 10^{-8.2}$ yr^{-1} and $\Sigma_{SFR} \sim 10^{-0.6} M_\odot$ kpc^{-2} yr^{-1}). This observational evidence supports the idea that region A is an active, young star-forming region found in NGC 3110. With the strong similarities of the observed gas and star formation properties with numerical minor merger simulations, we suggest that the ongoing interaction with the companion galaxy MCG-01-26-013 is the main driver of the star formation in region A, together with the central starburst activities.

To further investigate the physical properties and the origin of the star-forming regions in the disk of NGC 3110, it is essential to understand the properties of giant molecular clouds, which are a site of star formation. This can be addressed with the current long-baseline capability of ALMA.

Appendix
Scatter Plots with Varying α_{CO}

We show the scatter plots including the KS relation, SFE versus spectral index, and SFE versus SSC density in Figure 8. The molecular gas masses are derived assuming a constant α_{CO} of $1.7\,M_\odot$ (K km s^{-1} pc^2)$^{-1}$ (see Section 4.2.3). In order to discuss how these plots change when we apply the spatially varying α_{CO}, we reconstruct these with $\alpha_{LTE}(T_{rot})$ in Figure 9. The number of data points decreases compared to Figure 8, as the $\alpha_{LTE}(T_{rot})$ estimate is limited for $^{13}CO(2–1)$ detected apertures. However, we confirm that the varying α_{CO} does not strongly affect the trends in region A that we discussed in the main text. Thus, both constant and varying α_{CO} measurements lead to the same conclusions of this paper.
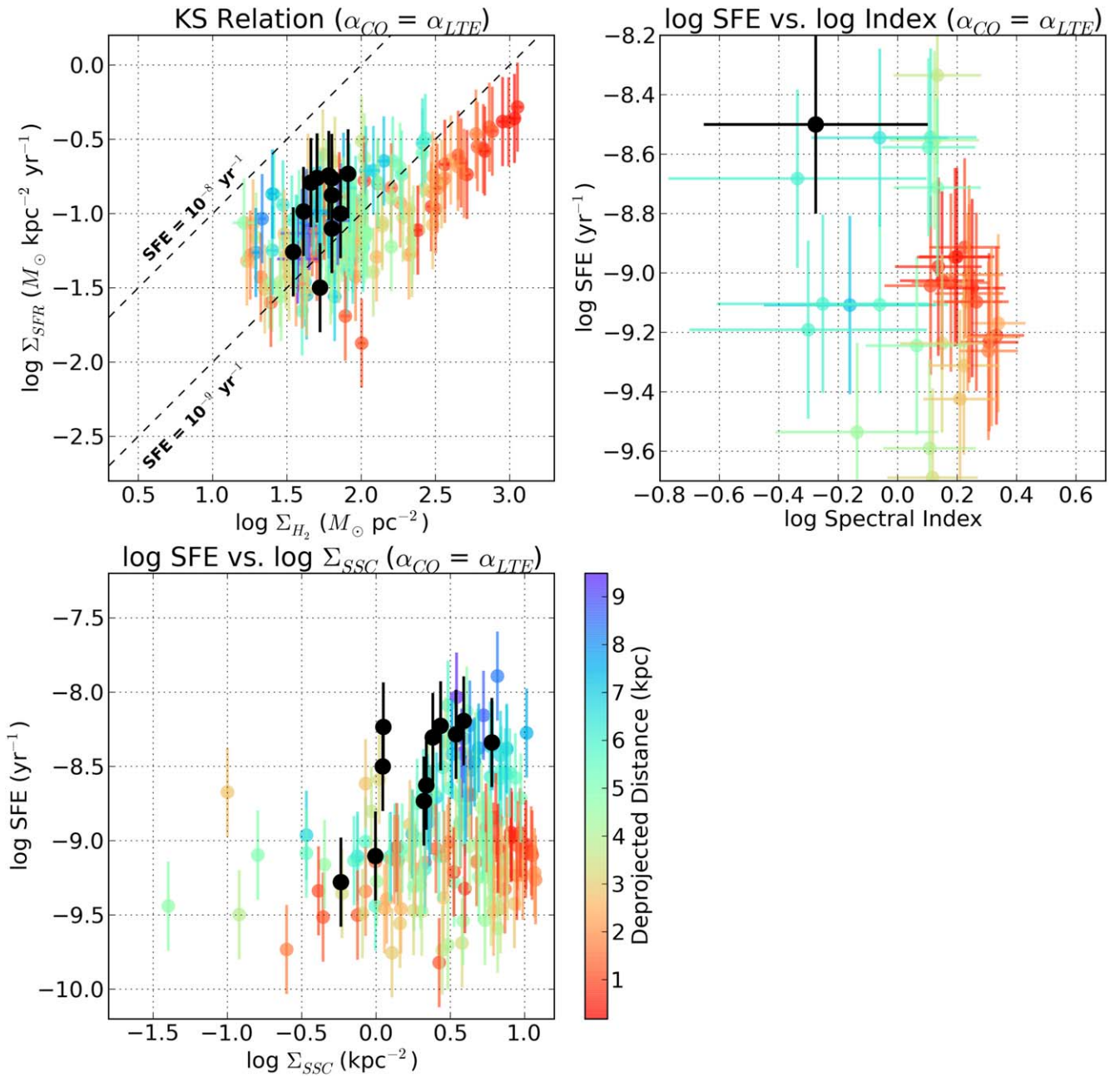
Figure 9. Same as the plots in Figure 8, but here we apply $\alpha_{\mathrm{LTE}}(T_{\mathrm{rot}})$ instead of a constant α_{CO} of 1.7 $M_\odot$ (K km s^{-1} pc^2)$^{-1}$.

ORCID iDs

Toshiki Saito ● https://orcid.org/0000-0002-2501-9328
Ryohei Kawabe ● https://orcid.org/0000-0002-8049-7525
Daniel Espada ● https://orcid.org/0000-0002-8726-7685
Daisuke Iono ● https://orcid.org/0000-0002-2364-0823
Hiroyuki Kaneko ● https://orcid.org/0000-0002-2699-4862
Minju M. Lee ● https://orcid.org/0000-0002-2419-3068
Tomonari Michiyama ● https://orcid.org/0000-0003-2475-7983
Kentaro Motohara ● https://orcid.org/0000-0002-0724-9146
Kouichiro Nakanishi ● https://orcid.org/0000-0002-6939-0372
Alex R. Pettitt ● https://orcid.org/0000-0002-3662-3942
Zara Randriamanakoto ● https://orcid.org/0000-0003-2666-4158

Junko Ueda ● https://orcid.org/0000-0003-3652-495X
Takuji Yamashita ● https://orcid.org/0000-0002-4999-9965

References

Armus, L., Mazzarella, J. M., Evans, A. S., et al. 2009, PASP, 121, 559
Astropy Collaboration, Robitaille, T. P., Tollerud, E. J., et al. 2013, A&A, 558, A33
Astropy Collaboration, Price-Whelan, A. M., Sipőcz, B. M., et al. 2018, AJ, 156, 123
Barnes, J. E., & Hernquist, L. 1992, ARA&A, 30, 705
Bigiel, F., Leroy, A., Walter, F., et al. 2008, AJ, 136, 2846
Blake, G. A., Sutton, E. C., Masson, C. R., & Phillips, T. G. 1987, ApJ, 315, 621
Bolatto, A. D., Wolfire, M., & Leroy, A. K. 2013, ARA&A, 51, 207
Condon, J. J. 1992, ARA&A, 30, 575
Cornwell, T. J. 2008, ISTSP, 2, 793

Cox, T. J., Jonsson, P., Somerville, R. S., Primack, J. R., & Dekel, A. 2008, MNRAS, 384, 386

den Brok, J. S., Chatzigiannakis, D., Bigiel, F., et al. 2021, MNRAS, 504, 3221

Downes, D., & Solomon, P. M. 1998, ApJ, 507, 615

Elmegreen, D. M., Elmegreen, B. G., Kaufman, M., et al. 2017, ApJ, 841, 43

Espada, D., Matsushita, S., Peck, A. B., et al. 2012, ApJL, 756, L10

Espada, D., Martin, S., Hsieh, P. Y., et al. 2010, in Galaxies and their Masks, ed. D. L. Block, K. C. Freeman, & I. Puerari (Cham: Springer), 97

Espada, D., Martin, S., Verley, S., et al. 2018, ApJ, 866, 77

Goldsmith, P. F., & Langer, W. D. 1999, ApJ, 517, 209

Hainline, L. J., Scoville, N. Z., Yun, M. S., et al. 2004, ApJ, 609, 61

Hattori, T., Yoshida, M., Ohtani, H., et al. 2004, AJ, 127, 736

Hubble, E. P. 1926, ApJ, 64, 321

Hunter, J. D. 2007, CSE, 9, 90

Iono, D., Yun, M. S., & Mihos, J. C. 2004, ApJ, 616, 199

Iono, D., Saito, T., Yun, M. S., et al. 2013, PASJ, 65, L7

Kaneko, H., Kuno, N., & Saitoh, T. R. 2018, ApJL, 860, L14

Kennicutt, Robert C., J. 1998a, ARA&A, 36, 189

Kennicutt, Robert C., J. 1998b, ApJ, 498, 541

Kennicutt, Robert C., J., Hao, C.-N., Calzetti, D., et al. 2009, ApJ, 703, 1672

Kennicutt, R. C., & Evans, N. J. 2012, ARA&A, 50, 531

Koda, J., Sawada, T., Sakamoto, K., et al. 2020, ApJL, 890, L10

Lacy, J. H., Knacke, R., Geballe, T. R., & Tokunaga, A. T. 1994, ApJL, 428, L69

Leroy, A. K., Walter, F., Brinks, E., et al. 2008, AJ, 136, 2782

Liu, D., Daddi, E., Schinnerer, E., et al. 2021, ApJ, 909, 56

Lundgren, A. 2013, ALMA Cycle 2 Technical Handbook Version 1.1, ALMA, https://arc.iram.fr/documents/cycle2/alma-technical-handbook.pdf

McMullin, J. P., Waters, B., Schiebel, D., Young, W., & Golap, K. 2007, in ASP Conf. Ser., 376, Astronomical Data Analysis Software and Systems XVI, ed. R. A. Shaw, F. Hill, & D. J. Bell (San Francisco, CA: ASP), 127

Mihos, J. C., & Hernquist, L. 1996, ApJ, 464, 641

Müller, H. S. P., Schlöder, F., Stutzki, J., & Winnewisser, G. 2005, JMoSt, 742, 215

Müller, H. S. P., Thorwirth, S., Roth, D. A., & Winnewisser, G. 2001, A&A, 370, L49

Nakajima, T., Takano, S., Kohno, K., Harada, N., & Herbst, E. 2018, PASJ, 70, 7

Oliphant, T. 2006, NumPy: A guide to NumPy (USA: Trelgol Publishing)

Pettitt, A. R., Tasker, E. J., Wadsley, J. W., Keller, B. W., & Benincasa, S. M. 2017, MNRAS, 468, 4189

Pettitt, A. R., & Wadsley, J. W. 2018, MNRAS, 474, 5645

Randriamanakoto, Z. 2015, PhD thesis, Univ. Cape Town

Randriamanakoto, Z., & Väisänen, P. 2017, in IAU Symp. 316, Formation, Evolution, and Survival of Massive Star Clusters, ed. C. Charbonnel & A. Nota (Cambridge: Cambridge Univ. Press), 70

Randriamanakoto, Z., Väisänen, P., Ryder, S., et al. 2013, MNRAS, 431, 554

Randriamanakoto, Z., Väisänen, P., Ryder, S. D., & Ranaivomanana, P. 2019, MNRAS, 482, 2530

Saito, T., Iono, D., Yun, M. S., et al. 2015, ApJ, 803, 60

Saito, T., Iono, D., Xu, C. K., et al. 2016, PASJ, 68, 20

Saito, T., Iono, D., Xu, C. K., et al. 2017, ApJ, 835, 174

Saitoh, T. R., Daisaka, H., Kokubo, E., et al. 2009, PASJ, 61, 481

Sanders, D. B., Scoville, N. Z., & Soifer, B. T. 1991, ApJ, 370, 158

Sandstrom, K. M., Leroy, A. K., Walter, F., et al. 2013, ApJ, 777, 5

Schöier, F. L., van der Tak, F. F. S., van Dishoeck, E. F., & Black, J. H. 2005, A&A, 432, 369

Scoville, N., Sheth, K., Aussel, H., et al. 2016, ApJ, 820, 83

Sliwa, K., Wilson, C. D., Iono, D., Peck, A., & Matsushita, S. 2014, ApJL, 796, L15

Sliwa, K., Wilson, C. D., Matsushita, S., et al. 2017, ApJ, 840, 8

Solomon, P. M., & Vanden Bout, P. A. 2005, ARA&A, 43, 677

Teyssier, R., Chapon, D., & Bournaud, F. 2010, ApJL, 720, L149

Tomičić, N., Hughes, A., Kreckel, K., et al. 2018, ApJL, 869, L38

U, V., Sanders, D. B., Mazzarella, J. M., et al. 2012, ApJS, 203, 9

van der Tak, F. F. S., Black, J. H., Schöier, F. L., Jansen, D. J., & van Dishoeck, E. F. 2007, A&A, 468, 627

Virtanen, P., Gommers, R., Oliphant, T., et al. 2020, NatMe, 17, 261

Watanabe, Y., Sakai, N., Sorai, K., & Yamamoto, S. 2014, ApJ, 788, 4

Whitmore, B. C., Zhang, Q., Leitherer, C., et al. 1999, AJ, 118, 1551